Optimal averaging of NOAA/NASA Pathfinder satellite sea surface temperature data

Alison E. Walker[1] and John L. Wilkin[2]

Division of Marine Research, Commonwealth Scientific and Industrial Research Organisation, Hobart, Tasmania
Australia

Abstract. Statistical interpolation is applied to 8 years of cloud-interrupted satellite radiometer data to produce estimates of sea surface temperature (SST) at 10-day intervals in the Indo-Australian region. The data are 9-km resolution daily "best SST" values calculated globally by the NOAA/NASA Pathfinder project reanalysis of advanced very high resolution radiometer (AVHRR) data. The optimal averaging technique determines an unbiased estimate of the signal that has the minimum mean square variance from the data, within the limits of the expected measurement error. Previous studies have shown that the method is superior to other linear averaging techniques, especially that of simple composite averaging. The method is applied in the time domain only, preserving the 9-km spatial resolution of the data. The signal and noise covariances were evaluated from the data. This was done with care so that accurate estimates of the error bounds that bracket the optimally averaged values might be obtained. These error bounds were then verified against in situ data. A Markov function, $(1 + \tau/a) \exp(-\tau/a)$, where τ is the time lag and a is a characteristic timescale, was fitted to the data and used for the signal correlation function. This was selected after evaluation of functional forms proposed in other studies. The effect on the analysis of geographical variation in the correlation function was considered. The computational demand of the repeated matrix operations in optimal interpolation was reduced by using a limited duration data window. The complete analysis procedure for the 8-year data set, comprising over 10^6 time series, was tractable on a modern workstation. The result is a set of SST maps for 1987–1994 at an interval of 10 days and a spatial resolution of 9 km. The analyses are suitable for applications such as high-resolution ocean and atmosphere modeling where the timescales and space scales of interest are comparable to the analysis (i.e., of the order of 10 days, 9 km) and for which the presence of gaps due to clouds is problematic. Some features of Indo-Australian regional mesoscale circulation that the analysis highlights are examined, including examples of detailed mesoscale SST evolution and interannual variability.

1. Introduction

Remotely sensed sea surface temperature (SST) data from the radiometers on board NOAA meteorological satellites are used widely in studies of the ocean. Clouds obscure radiometer SST observations, and this is problematic for applications where an uninterrupted high-resolution SST data set is required. Cloud detection algorithms help minimize data loss, but the gaps created by cloud cover often must be filled by time and space averaging or interpolation. This paper describes the application of a statistical interpolation/averaging method to produce uninterrupted SST maps with a spatial resolution of 9 km and temporal separation of 10 days. The results are suitable as boundary conditions for high-resolution regional models of the ocean and atmosphere, and they also directly chart interannual variability and readily locate repetitive mesoscale features and the timescales and space scales of their residence and reappearance.

[1]Now at Woods Hole Oceanographic Institute, Woods Hole, Massachusetts.

[2]Now at School of Environmental and Marine Sciences, Tamaki Campus, University of Auckland, Auckland, New Zealand.

The input data for the analysis are the daily, ~9-km resolution, "best SST" data from the NOAA/NASA Pathfinder Project reanalysis of advanced very high resolution radiometer (AVHRR) data [Smith et al., 1996]. These are global, multichannel data sets derived from the global area coverage (GAC) data acquired by the AVHRR instruments onboard the NOAA TIROS polar-orbiting meteorological satellites. Features of these data and a synopsis of the Pathfinder reanalysis procedure are given in section 2.
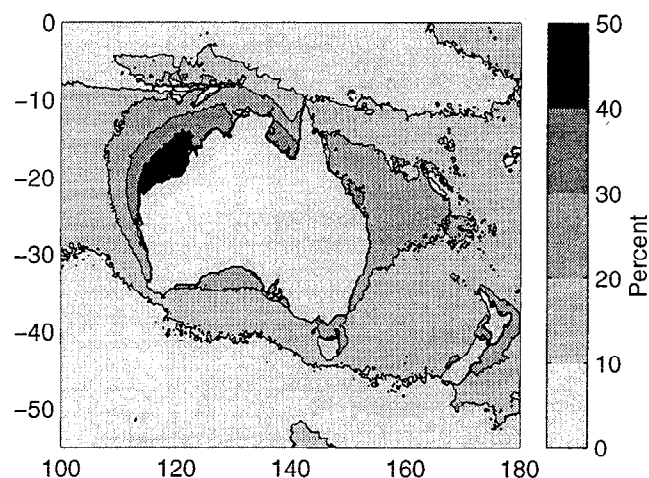
In section 3 the mean seasonal cycle and long-term trends of the data are determined, and some features of the regional circulation that they show are discussed. The optimal (statistical) interpolation formulation is reviewed in section 4. It is applied in the time domain only, thereby retaining the 9-km spatial resolution. The inclusion of time averaging follows that employed by Chelton and Schlax [1991] in their estimation of time averages of chlorophyll concentration from the coastal zone color scanner (CZCS). They proved statistical interpolation to be a significant improvement upon the simple composite averaging used by many workers to estimate several-day averages from data with gaps resulting from clouds. Successful application of the method relies on the removal of slowly varying background time series (taken from section 3) and the estimation of certain properties of the residual time series to

Figure 1. The percentage of days for which best sea surface temperature (SST) data are recorded in each Pathfinder time series for 1987–1994.

be interpolated. The basis of our choice of these parameters is presented in section 5.

A comparison with in situ data in section 6 serves two purposes: ensuring that no outrageous biases occur in the satellite data and verifying the accuracy of the theoretical error estimates produced in the analysis. The method is applied in the regional seas surrounding Australia to produce 10-day SST maps for the entire period of Pathfinder data available to us. In section 7, examples of the results illustrate the types of mesoscale structures that the analysis resolves.

2. Pathfinder SST Data Set

The Jet Propulsion Laboratory (JPL) Physical Oceanography Distributed Active Archive Center (PO.DAAC) make available a great range of data products, of which we have chosen the equal angle $(360/2^{12}$ degrees of arc), nominally 9-km resolution, global best SST data spanning the period January 1987 to August 1994. The steps involved in producing these data are described in detail by *Smith et al.* [1996] and by JPL PO.DAAC (the NOAA/NASA AVHRR Oceans Pathfinder home page, available as http://podaac.jpl.nasa.gov/sst/). The quality of the original 4-km GAC data downloaded from the spacecraft is flagged according to certain multichannel and threshold tests. Further cloud clearing is achieved by comparison to climatology and triweekly averages. In addition to clouds, AVHRR measurements are subject to errors from aerosol contamination. An example would be the large negative biases associated with stratospheric aerosols from the Mount Pinatubo eruption in June 1991 [*Reynolds*, 1991]. The bias, or mean difference of AVHRR minus in situ SST value, in this case reached −1.5°C. However, careful incorporation of in situ measurements can correct for these types of atmospheric anomaly. The Pathfinder algorithm utilizes a matchup data base of in situ SST observations to adjust the coefficients of the nonlinear SST algorithm.

A comparison of version 1 Pathfinder SST with matchup data from moorings and buoys for 1987–1990 (E. Smith, personal communication, 1997) (available as http://www.ccpo.odu.edu/~lizsmith/) showed a global average bias of −0.1°C and a root-mean-square (rms) difference of 0.94°C. The negative

bias suggests that there may still be some cloud contamination in the Pathfinder data set [*Smith et al.*, 1996].

Our region of interest is from the equator to 70°S and 90°E to 160°W, which spans approximately one eighth of the ocean surface. We choose to use as input to our analysis only the descending satellite passes, as these occur during the early morning hours for this region and as such should be less affected by diurnal heating. The number of time series involved is then of the order of 10^6.

The 8-year data set spans 2780 days; however, the maximum number of best SST values at any one location is just 50% of the total and on average is between 10 and 20% (Figure 1). This fraction can be thought of as a negative cloud index. It is shown in section 5 that regions of higher data availability, in general, have a lower predicted error in the estimated SST.

3. Mean Seasonal Cycle

It is preferable to apply statistical interpolation to the anomaly time series when as much background deterministic long-timescale variability as possible has been removed. This background is restored after interpolation. In this way the anomaly series is more likely to meet the condition of being statistically stationary, and in prolonged data gaps when the interpolation returns an estimate near zero, the final estimate produced will approach the background field or, effectively, climatology.

We chose to determine the background field for each time series independently by least squares fit to the sum of a mean and by annual and semiannual period harmonics. Longer-term climatology was estimated by a 365-day running mean. The fitted parameters show coherent spatial patterns throughout (Plate 1).

The geographical structure apparent in Plates 1a–1f, resolved to 9 km, carries a wealth of information. Sharp V-shaped patterns in the mean isotherms adjacent to the west and east coasts of Australia are the signatures of two warm southward flowing boundary currents. In the west the extension of the Leeuwin Current turns at Cape Leeuwin toward the Great Australian Bight, where it continues to warm shelf waters with respect to those offshore. In the east the East Australian Current (EAC) carries warm Coral Sea water southward along the outer edge of the Great Barrier Reef. At 35°S, where the V-shaped pattern weakens, the EAC turns toward New Zealand. In the eastern Tasman Sea the 17°–18°C isotherms meander southward, then northward, as they cross the Caledonia Basin and Wanganella Bank (depth <500 m) on the crest of Norfolk Ridge. A strong meander in subsurface thermal data and intensified velocities have been observed there and are associated with topographic deflection of eastward flow [*Stanton*, 1976, 1979]. Isotherms strike southward along the northeast coast of New Zealand, where the East Auckland Current flows southward. In the southwest corner of Plate 1a, surface isotherms converge along a line from 95°E, 45°S to 120°E, 50°S, paralleling the northern flank of the Southeast Indian Ridge and revealing a surface signature of the Subantarctic Front [*Belkin and Gordon*, 1996].

Plates 1b and 1c show that large annual temperature variations are the norm on the continental shelf, with the phase of the maximum occurring at the peak of summer in January or February. In a broad region of the northeast Indian Ocean between the northwest shelf of Australia and Java the month of warmest temperature occurs successively later, from Janu-

ary near Timor through to April west of 105°E, as tropical waters spread southwestward during this season [*Gentilly*, 1972]. In a narrow region close to the coast of western Australia, from 22° to 35°S, the annual cycle peaks in April, much later than the surrounding offshore waters. It is at this time of year that the Leeuwin Current is at its strongest, bringing warm waters from the tropics [*Cresswell and Golding*, 1980; *Godfrey*, 1996].

Some local regions of low annual amplitude can be distinguished. At the southwest corner of the mainland, weak southerly winds during May allow the Leeuwin Current extension to advect warm water around Cape Leeuwin, sometimes at speeds of up to 1.5 m s^{-1} [*Tomczak and Godfrey*, 1994], offsetting the wintertime cooling that would otherwise occur. Another region of low annual amplitude is in the east of the Great Australian Bight, where summer upwelling regularly brings cooler water to the surface, thereby decreasing the amplitude of the seasonal cycle [*Schahinger*, 1987].

Significant semiannual SST variation (Plate 1d) only occurs close to shore along Australia's northern coast and in the Banda Sea, where the cycle peaks in April and October, at times of weak monsoon winds. Elsewhere, the calculated semiannual signal is weak, and little relevance can be ascribed to its phase (not shown).

After the mean seasonal cycle was removed from each time series a 365-day running mean filter was applied to the residuals to determine the interannual component of the background climatology. Plate 1e shows the standard deviation of this component over the 8 years of data. Interannual variability is greatest in the western equatorial Pacific, where large SST changes are related to El Niño–Southern Oscillation (ENSO) events. There are other regions of notable interannual variability. Along the south coast of Java the SST minimum that occurs each September because of upwelling during the southwest monsoon is about 1°C colder than normal in the years 1987, 1988, and 1994 (and, to a lesser extent, 1991). Interannual variation south of the Great Australian Bight is in the form of a warming of some 2°C over the years 1987–1990. In the east Tasman Sea and subtropical waters surrounding northern New Zealand, there is a cycle of amplitude ±0.5°C of roughly 7-year period, with minimum during winter 1992, that is similar to the cycle observed by *Sprintall et al.* [1995] in expendable bathythermograph (XBT) data. They attributed the variability to divergence in the upper 200-m heat budget in the region and related this to anomalous cold atmospheric conditions in New Zealand in winter 1992. In our data the cycle appears to be locally amplified at Wanganella Bank (±1°C), where *Stanton* [1979] found that the location of the Tasman Front varied significantly between years.

Once the cyclic seasonal and interannual background field is removed from each time series the variance of the anomaly data (Plate 1f) is a measure of the signal, plus noise, remaining to be described by the optimal interpolation. This variability is predominantly at shorter timescales than the seasonal cycle. High variance occurs where there is known mesoscale eddy activity; in the region from the EAC separation southward to Tasmania and in the Leeuwin Current and its extension around Cape Naturaliste. There is also high variance along the axis of the Subantarctic Front owing presumably to meandering of the front's location. The fitted background field accounts for >85% of SST variance in the Australian regional seas.

4. Optimal Averaging of Irregularly Sampled Time Series

The methodology we use has been described previously in the oceanography literature, where it is variously referred to as Gauss-Markov, optimal or statistical interpolation, or objective analysis [*Gandin*, 1963; *Bretherton et al.*, 1976]. The technique is commonly used to interpolate irregularly sampled, noisy data to regular grids for subsequent analysis. Here we apply the method solely in time and preserve the high spatial resolution of the data. The analysis is therefore somewhat akin to digital filtering in time series analysis but with explicit account being taken of measurement error in the data. Our principal objective is to overcome gaps in the time series and construct a set of smoothed time series of SST at the shortest meaningful regular intervals.

After removing the background seasonal cycle each anomaly time series may be denoted θ_k, $k = 1, \cdots, N$, comprising N inexact observations made at times t_k.

$$\theta_k = \phi_k + \varepsilon_k \tag{1}$$

These data are the sum of two, assumed independent, stationary stochastic processes, the signal ϕ_k and noise ε_k, that we wish to separate. The optimal estimate $\hat{\phi}$ of the true value ϕ at any given estimation time t_0 will be calculated as a weighted sum of the data

$$\hat{\phi}(t_0) = \sum_{k=1}^{N} \alpha_k \theta_k \tag{2}$$

where the weights α_k will be different at each estimation time. The noise is assumed to be uncorrelated with itself and to have variance σ_e^2

$$\overline{\varepsilon_i \varepsilon_j} = \sigma_e^2 \delta_{ij} \tag{3}$$

where the overbar denotes the expected value. The signal covariance is

$$\overline{\phi_i \phi_j} = \sigma_\phi^2 \rho_{i,j} \tag{4}$$

where σ_ϕ^2 is the signal variance, and time stationarity implies that the normalized correlation function $\rho_{i,j} = \rho(\tau_{i,j})$ is symmetric and invariant, depending only on the time lag $\tau_{i,j} = |t_i - t_j|$.

The Gauss-Markov formulation minimizes the expected ensemble mean square error of the interpolation in a least squares sense, giving a set of linear equations for the α_k

$$(\mathbf{P} + \lambda \mathbf{I})\alpha = \tilde{\rho} \tag{5}$$

where $\mathbf{P}$ is the signal correlation matrix with elements $P_{ij} = \rho(\tau_{i,j})$, $\mathbf{I}$ is the identity matrix, and $\lambda = \sigma_e^2/\sigma_\phi^2$ is the ratio of noise to signal variance. The right-hand side of (5) is a vector of the time average of the signal correlation over an averaging period T, with elements

$$\tilde{\rho}_i = \frac{1}{T} \int_{t_0 - T/2}^{t_0 + T/2} \rho(t' - t_i) \, dt' \tag{6}$$

Chelton and Schlax [1991] introduced the notion of time averaging to the standard optimal interpolation method in recognition that some temporal averaging is desirable to reduce the aliasing of high-frequency variability in the signal. Consequently, the quantity that is estimated is not the signal at a

particular estimation time but is its average over an interval T chosen to be relevant to the application and available data density. This is an important point to remember when comparisons with *in situ* data are performed in section 6.

The theoretical estimate of the mean square error in the analysis ψ^2 is given by [*Chelton and Schlax*, 1991]

$$\psi^2 = \sigma_\phi^2 (\gamma - \boldsymbol{\alpha}^T \tilde{\boldsymbol{\rho}})$$

$$\gamma = \frac{1}{T^2} \int_{t_0-T/2}^{t_0+T/2} \int_{t_0-T/2}^{t_0+T/2} \rho(t' - t) \, dt' \, dt \qquad (7)$$

The correlation function ρ, signal-to-noise ratio λ, and averaging period T must be specified prior to applying the method. Our procedure for choosing these is shown in section 5 along with a discussion of the theoretical error estimates.

5. Application to the Pathfinder Data

In principle the correlation function and signal-to-noise ratio must be estimated accurately for the result to be optimal. However, we need not be overzealous as derived estimates are sufficiently robust that a reasonable guess of suboptimal parameters produces estimates that do not significantly differ from the optimal parameter estimates [*Chelton and Schlax*, 1991; *Denman and Freeland*, 1985]. Where sampling is well distributed, the change in patterns is negligible.

5.1. SST Correlation Function

The correlation of the SST data was estimated by calculating the mean of anomaly data covariance values $\theta_i \theta_j$ binned according to lag. A continuous functional form was then sought that closely represented the shape of the observed data correlation, with the parameters of the function being determined by least squares fit. In most applications of optimal interpolation the Gaussian function has been favored as the shape of the correlation function, although many other functions have been considered. The performance of optimal interpolation using varied correlation functions has been examined through the use of synthetic data where the statistics are known [*Franke*, 1985] and through the use of real data where certain locations are withheld [*Seaman and Hutchinson*, 1985].

We considered three single parameter functional forms for $\rho(\tau)$ used in recent studies and compared their ability to represent the following sample SST correlations: (1) Gaussian, $\rho(\tau) = \exp\left[-\frac{1}{2}(\tau/a)^2\right]$; (2) linear roll-off in the power spectrum, $\rho(\tau) = $ inverse Fourier transform of ω^{-a}, where ω is frequency [*Chelton and Schlax*, 1991]; and (3) Markov, $\rho(\tau) = (1 + \tau/a) \exp(-\tau/a)$, $\tau > 0$ [*Seaman and Hutchinson*, 1985].

The parameter a is in each case a measure of the timescale of correlation. The shortcomings of the Gaussian function when applied to typical geophysical data can be summarized as a propensity to overestimate the weights α_k at short lags and underestimate them at large lags [*Franke*, 1985; *McIntosh*, 1990]. This amounts to oversmoothing at small scales and may be countered by artificially lowering the value of λ, causing the interpolation to follow the data more faithfully. The second function is based on a constant roll-off of slope a in the power spectrum. *Chelton and Schlax* [1991] found that $a = 1.35$ fit log-transformed chlorophyll data well. Fitting to the Pathfinder
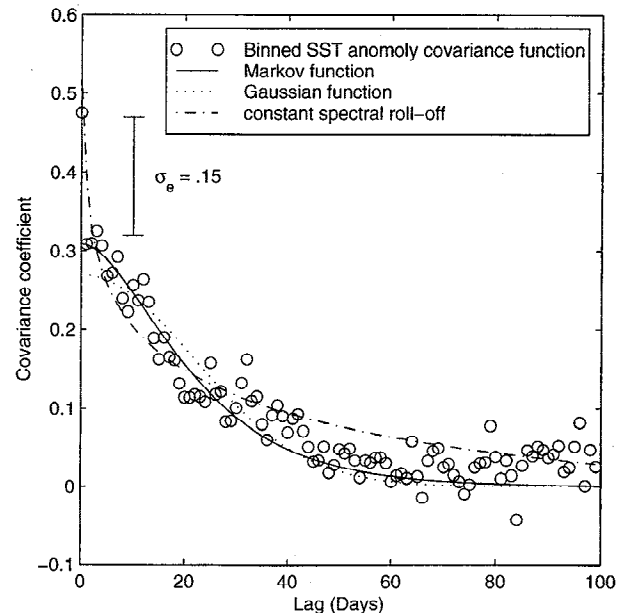
Figure 2. Three functional forms for the correlation function fitted to the binned lagged covariance for best SST data in the Coral Sea (160°E, 25°S).

data gave values near $a = 0.5$, but the function tended to fall off too sharply for the short lag correlation. The three functions were fitted to sample binned lag covariances within our data region; a typical example is shown in Figure 2. We found that the Markov function fitted the shape of the Pathfinder SST correlation best throughout our region of interest, and we use it for all our analyzed time series.

The optimally averaged estimates corresponding to the differing functional fits of Figure 2 are shown in Figure 3. For the most part the three functions give similar optimal estimates, there being only occasional instances where they differ by more than the expected error $\pm\psi$. The linear spectral roll-off function shows a propensity to drop to an estimate nearer zero during data gaps, a consequence of the weights falling more rapidly at shorter lags. Also, the larger weights placed on the very close range data cause the interpolation to reach toward individual data values. The Gaussian function produces an overall smoother estimate.

5.2. Signal-to-Noise Variance Ratio

To estimate the measurement error variance, we utilize the assumption that the noise is uncorrelated with itself. The data covariance should therefore comprise the signal covariance plus a delta peak at zero lag due to the noise. The data variance at zero lag (Plate 1f) is then $\phi_i^2 = \sigma_\phi^2 + \sigma_e^2$. This property is evident in Figure 2; close to zero lag, the covariance function approaches a signal variance of $0.32°C^2$, yet the data variance jumps to $0.47°C^2$ at zero lag, indicating a noise variance of the order of $0.15°C^2$. This corresponds to a measurement error of $0.39°C$, which is less than the commonly accepted measurement error of the order of $0.6°C$ in AVHRR data. This is presumably a result of the 9-km spatial averaging and strict quality control of the Pathfinder data.

The value $\sigma_e^2 = 0.15°C^2$ was found to be appropriate throughout the region, so that the signal-to-noise variance ratio λ was computed directly from the anomaly variance at each point as
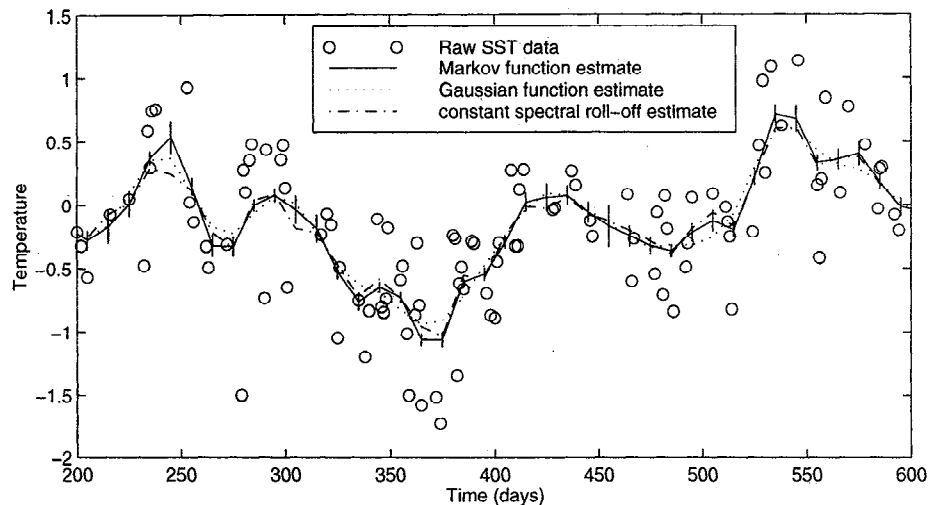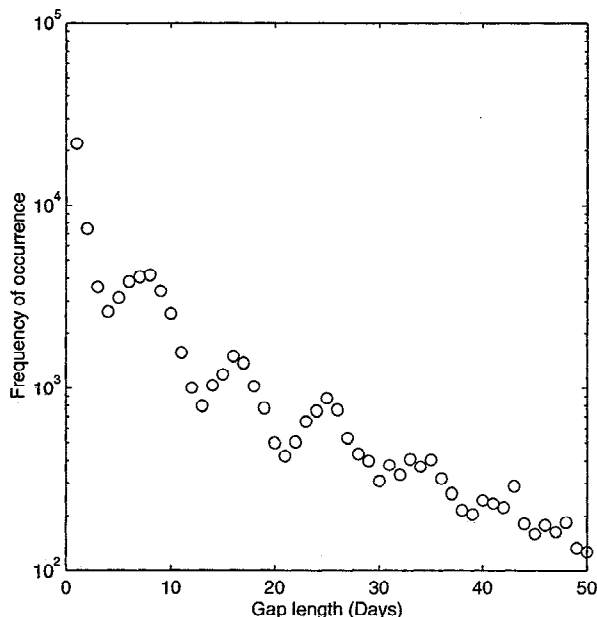
Figure 3. Optimally averaged time series and best SST data corresponding to the three forms for the correlation function in Figure 2.

$$\lambda = \sigma_e^2/\sigma_\phi^2 = \sigma_e^2/(\overline{\phi_i^2} - \sigma_e^2) \qquad (8)$$

5.3. Averaging Time Period

Cloudiness that obscures satellite SST observations may persist for many days. Figure 4 shows the frequency of occurrence of a given gap for a set of time series at 10°S across the central Coral Sea. The periodic signal that is evident is a function of satellite trajectory and the width of the satellite's field of view and is most pronounced at low latitudes but no longer discernible by midlatitudes. The underlying log decay in gap duration is representative of all locations, and for most of the Pathfinder data, 90% of adjacent data points are separated by less than 4 days.

Temporal averaging was introduced to the interpolation procedure to smooth high-frequency signal variability. To reduce the possibility of aliasing high frequencies, an averaging time period of $T = 10$ days was chosen so that the majority of data gaps are shorter than $T/2$.
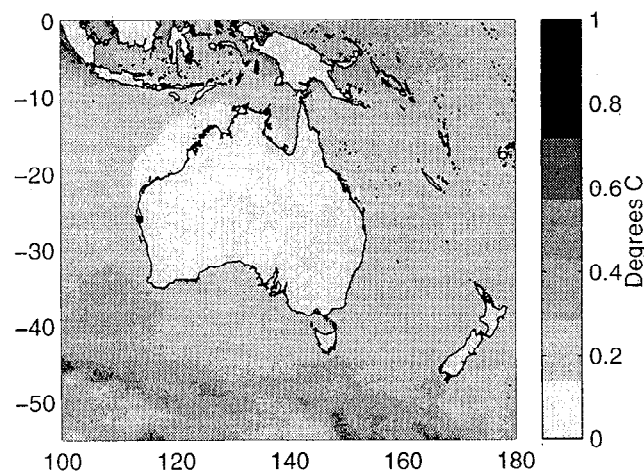
Throughout most of our region of interest the maximum gap is <40 days. However, equatorward of 10°S and in the southern Indian Ocean, the maximum gap can be quite extreme. This would preclude the use of many interpolation methods which may otherwise be faster; a running average may have to stretch to a length of 100 days to find a data value, and smoothing based on polynomial functions may produce estimates well outside the bounds of reasonable values where large data gaps fail to constrain the smoothing functions.

5.4. Theoretical Mean Square Error Estimation

The mean square error in any optimal average ψ^2 is given by (7). It is proportional to the signal variance σ_ϕ^2 but is dependent on the individual data points only in terms of the data spacing and the chosen ρ and λ, not the individual data values themselves.

The estimated ψ^2 may be quite misleading when an inaccurate representation of the correlation function is used [*Franke*, 1985; *McIntosh*, 1990]. *McIntosh* [1990] gives an example where the correlation length scale is greater than the true value and the actual interpolation error increases while the estimated error decreases. This is because the optimal interpolation method is instructed to place greater weight on more observations in the belief it can interpolate more accurately, whereas in fact, it fails to resolve variability at the true length scale. He concluded that it is best to underestimate the length scale in uncertain cases.

Given the care with which we have estimated ρ and λ, we have confidence that the error estimates included with the 10-day optimal average results in section 7 are reasonable. This is attested to in the comparisons with in situ data in section 6. The median ψ for each time series (Figure 5) shows that at midlatitudes, where the Pathfinder data has the fewest gaps, the median expected error in the optimal averages is typically 0.2°C.

Figure 4. The frequency of the occurrence of gaps of particular duration in the best SST time series at 10°S in the central Coral Sea. The data are nominally daily, so a gap of 1 day corresponds to an uninterrupted time series.

Figure 5. Median expected error for each time series $\pm\psi$ from (7).

5.5. Processing the Full Data Set

The method is formulated assuming the optimal average is a weighted sum of all the data in the time series, but in practice, the analysis can be restricted to an appropriate duration on either side of the estimation time because at large lags the α_k values become very small. This lessens the computational load by reducing the dimension of the matrices in (5). We chose an 80-day data window centered on the estimation time. The matrices in (5) are sized by the number of best SST values in the data window and thus vary for each estimate time, being typically of the order of 15.

Over a region of interest as large as that considered here, the correlation function might be expected to vary as the physical processes that influence SST variability and their timescales alter. Binned data correlations were compared for several locations within our region of interest (Figure 6) with each representing a different dynamical regime or regional situation: locations 1 and 4, subtropical convergence; location 2, Great
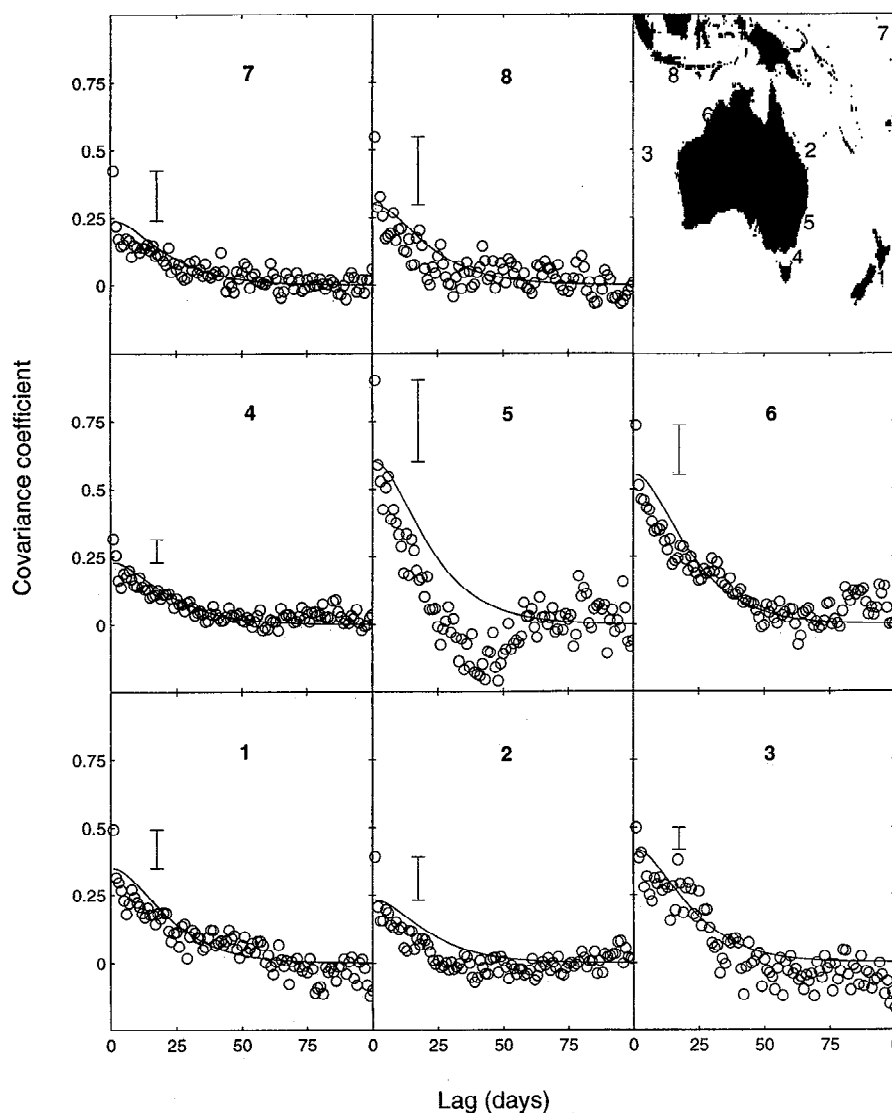
Figure 6. Binned lagged data covariance $\overline{\phi_i\phi_j}$ for several locations in the region of interest. The locations selected span the extremes of geographical variation in correlation timescale. Each plot shows the single Markov function, with $a = 12$, that was used in the final processing of all the optimal average time series. The bars in the left of each box show the amplitude of the delta peak at zero lag, which is equivalent to the noise variance. The locations pertaining to each number are also shown in Figure 6 (top right).
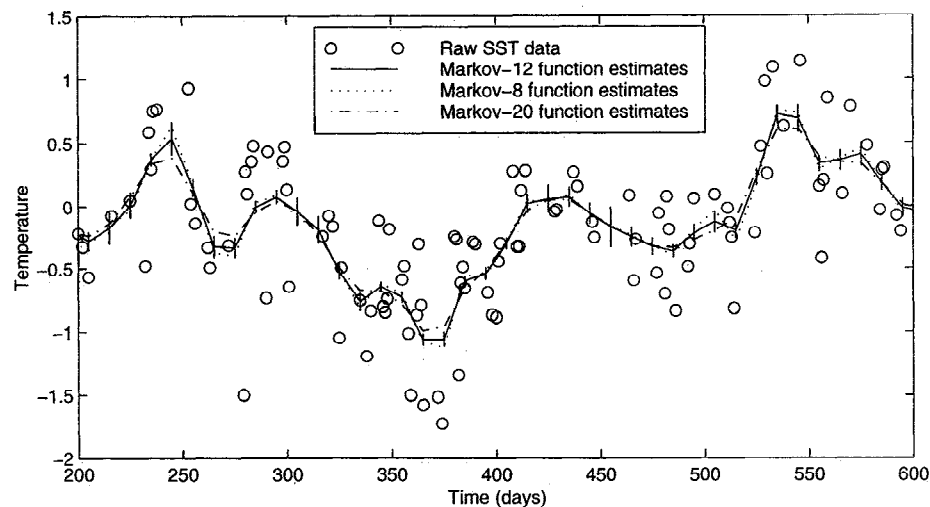
Figure 7. Optimally averaged time series for a location in the Tasman Sea computed using a Markov correlation function with $a = 12$ days (i.e., the value used to process the entire data set) and values $a = 8$ and 20 days that bracket the extremes of the timescales observed in the data. Expected error bounds are shown on the $a = 12$ time series.

Barrier Reef; location 3, midlatitude open ocean; locations 4 and 5, western boundary current; location 6, eastern boundary shelf; location 7, equator; and location 8, monsoon region. Over such a variety of regimes the shape and timescale of the correlation vary remarkably little. Therefore we elected to use a single Markov function, as its shape is most representative of the data (Figure 2), with timescale $a = 12$ days, to compute optimal averages for the entire data set. This one function is plotted in each panel of Figure 6 for comparison.

The poorest fit is at location 5, where there is a significantly negative correlation at 40–50 days, indicating a weak periodicity at 90 days in the East Australian Current system, a property also evident in velocities estimated from ship drift data [*Bennett*, 1983]. Elsewhere, the Markov function with $a = 12$ days fits well.

The timescale was calculated by least squares fit of the Markov function to the data correlation for lags <50 days. Throughout the entire region, best fits gave values of a typically between 11 and 13 days. To emphasize the stability of the optimal averages with respect to changes in a, Figure 7 compares results for $a = 12$ to those for $a = 8$ and 20 days (values that bracket the extremes we observed in the data) for a time series in the Tasman Sea. Results never differ by >0.2°C and for the most part are <0.05°C and well within the estimated error bounds on the $a = 12$ results. It may be useful to compare Figure 7 with Figure 3, which showed estimates using different functions rather than different length scales.

6. Validation of the Estimates Against in Situ Data

To evaluate the accuracy of our Pathfinder SST 10-day averages and error estimates, we compare them to three different types of in situ observations. These are surface conductivity-temperature-depth (CTD) observations from a single ship cruise, a set of drifting buoy observations, and continuous surface mooring readings spanning several years. A comparison would be best performed with in situ data that is also a 9-km 10-day average. The mooring data can be 10-day low-pass

filtered to remove higher-frequency variability, but for the ship and drifter data this is not possible because of the moving platforms. For these data we must accept that spatial and high-frequency temporal variability may add to the calculated variance between the optimal averages and in situ measurements.

The comparison is quantified by considering three criteria: (1) the mean bias between Pathfinder and in situ observations, (2) the root-mean-square (rms) difference between the 10-day averages and the in situ data compared to the theoretical value (rms_T) derived from the error estimates ($\pm \psi$), and (3) a chi-square goodness-of-fit test of the error estimates [*Bendat and Piersol*, 1966]. The chi-square test examines whether the proportion of in situ observations that fall within the estimated 10-day average error bars is consistent with the probability distributions of the data and the Pathfinder averages.

6.1. Drifting Buoys

Pathfinder 10-day averages were compared with coincident observations from nine drifting buoys released in the Australian regional seas by the Commonwealth Scientific and Industrial Research Organisation (CSIRO) during 1987–1994 (G. Cresswell, personal communication, 1997) (Table 1). The mean bias of the nine buoys was −0.02°C, and the rms difference between all observations and the analyses was 0.59°C. Of the nine buoys, only three have time series long enough to conduct a meaningful chi-square test. Their time series and the corresponding Pathfinder values and error bars are shown in Figure 8. For buoys 6140b and 6143b, more than 70% of the in situ observations lie within the estimated error bars, and the rms and rms_T values are similar (Table 2). The chi-square test indicates that for these two buoys the estimated error bars are a valid representation of the errors in the 10-day averages. (Degrees of freedom for the chi-square test were determined following *Bendat and Piersol* [1966, section 4.6], and the test was applied at the 95% significance level.)

The estimated errors in the Pathfinder analyses for buoy 6135b failed the chi-square test, largely because the final 6 months of the buoy data show a consistent bias of some −0.5°C

Table 1. Comparison of SST Observed by Drifting Buoys and Pathfinder Analysis Estimates

|	Start		End		Bias, °C	rms, °C
Buoy	Date	Position	Date	Position		
6130	Dec. 6, 1991	23.0°S 159.4°E	April 15, 1991	25.2°S 162.9°E	0.29	0.55
6131a	June 11, 1987	30.3°S 113.3°E	Dec. 31, 1987	27.7°S 108.3°E	−0.26	0.48
6135b	June 26, 1989	15.6°S 120.5°E	Dec. 31, 1990	12.0°S 73.9°E	−0.08	0.47
6138a	July 14, 1988	35.5°S 152.3°E	Feb. 20, 1989	25.0°S 153.3°E	−0.01	0.68
6139	Nov. 16, 1988	35.9°S 151.5°E	April 25, 1989	40.1°S 154.5°E	−0.03	0.63
6140b	Aug. 15, 1991	44.0°S 150.0°E	Dec. 7, 1993	39.7°S 172.5°E	0.01	0.53
6143b	July 30, 1992	42.0°S 144.7°E	May 29, 1994	38.5°S 169.8°E	0.02	0.60
6146b	May 26, 1992	42.7°S 148.8°E	Nov. 13, 1993	36.9°S 160.6°E	0.17	0.90
6150	April 29, 1993	12.6°S 129.9°E	Sept. 8, 1993	12.1°S 130.3°E	−0.30	0.43
Average over all buoys[a]					−0.02, $\sigma = 0.19$	0.59, $\sigma = 0.14$

[a]Here σ is standard deviation between buoys of the bias.

(Figure 8). We have no explanation why the first year of data from this buoy should compare well, yet the final 6 months compare so poorly. We would not have expected any significant change in the Pathfinder data over this period while the buoy traversed nearly due westward in the tropical Indian Ocean.

Buoy 6140b, which spent time south of Tasmania and in the Tasman Sea, covers the time period following the Mount Pinatubo eruption. It shows no sign of anomalously large bias that would indicate possible aerosol contamination.

6.2. CTD Cruise

Cruise FR9306 of the R/V *Franklin* transected the Tasman and Coral Seas in July, 1993 (J. Church, personal communication, 1997). The Pathfinder optimal averages for this period were linearly interpolated in time to the dates of the hydrographic stations and compared to the surface temperature recorded by the CTD (Figure 9). Though variability on short timescales and space scales cannot be filtered out of the CTD data, the comparison is very favorable.
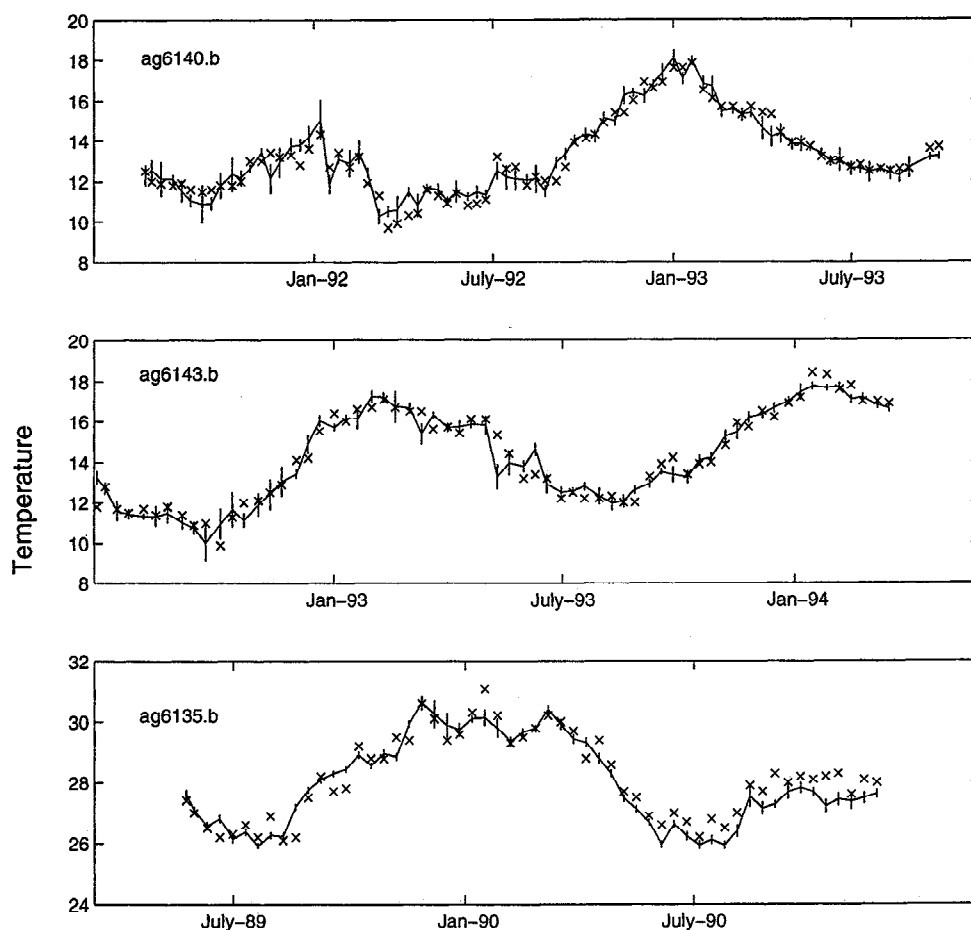
Figure 8. SST from three surface drifting buoys compared to 10-day Pathfinder averages interpolated to the buoy observation times. Buoy deployment and recovery locations are given in Table 1.

Table 2. Validation of 10-Day Average Pathfinder SST and Error Estimates by Comparison to Various In Situ Data

In Situ Observations	Bias, °C	rms, °C	rms_T, °C	Observations,[a] %	χ^2 Goodness-of-Fit Test		
					Sample Statistic[b]	n	Pass/Fail
Buoy 6135b	−0.08	0.47	0.18	41	297	5	fail
Buoy 6140b	0.01	0.49	0.44	78	4.75	5	pass
Buoy 6143b	0.02	0.56	0.40	72	4.33	5	pass
FR9306	−0.10	0.42	0.38	60	7.2	5	pass
TAO 5°S, 165°E	−0.27	0.41	0.35	45	16.8	9	pass

[a]Percent of observations that fall within expected error bars $\pm \psi$.

[b]Sample statistic [Bendat and Piersol, 1996, equation (4.49)] is compared to $\chi^2_{n;0.05}$, where n is the degrees of freedom.

The mean bias of −0.1°C is identical to the global average validation estimate noted in section 2. The rms difference was 0.47°C, which reduces to 0.42°C if the analysis estimates are first smoothed with a 1-2-1 time filter. This suggests that there is possibly some high-frequency error variance still in the analyses. In comparison, the average predicted error (rms_T) of the analyses is 0.38°C. Of the 79 CTD measurements, 60% lie within the error bars of the analysis estimates, and the error estimates pass the chi-square test.

6.3. Mooring Time Series

Figure 10 shows the 10-day Pathfinder averages compared to time series of 10-day low-pass-filtered daily average SST from the Tropical Atmosphere-Ocean (TAO) mooring (see NOAA/Pacific Marine Environmental Laboratory (PMEL) TAO home page, available as http://www.pmel.noaa.gov/toga-tao/) at 5°S, 165°E. The Pathfinder estimates fall below the TAO data in mid-1991 and do not recover until early 1992. This is almost certainly a bias related to the Mount Pinatubo eruption of June 1991. A second comparison to a TAO mooring on the

equator at 170°W (not shown) exhibits a Mount Pinatubo bias of similar magnitude and duration.

The 5°S, 165°E mooring time series has a mean bias of −0.43°C and a rms error of 0.63°C. If the 9 months following the Mt Pinatubo eruption are excluded, these drop to −0.29° and 0.43°C, respectively. The error bars pass the chi-square test if the anomalous 9 months are excluded. Thus, while the error bars adequately represent the typical error variance, they cannot accommodate such a major systematic bias as the Pinatubo eruption.

6.4. Diurnal Variation

Diurnal SST variations can be substantial where low-wind conditions permit shallow mixed layer depths and insolation is strong. The Pathfinder analyses computed here are based on nighttime measurements, which are typically the lowest values in the daily cycle, and therefore could possibly show a negative bias of around one half the value of the average diurnal cycle. From midlatitudes to the Southern Ocean we do not expect this to be a major consideration in the present data because of
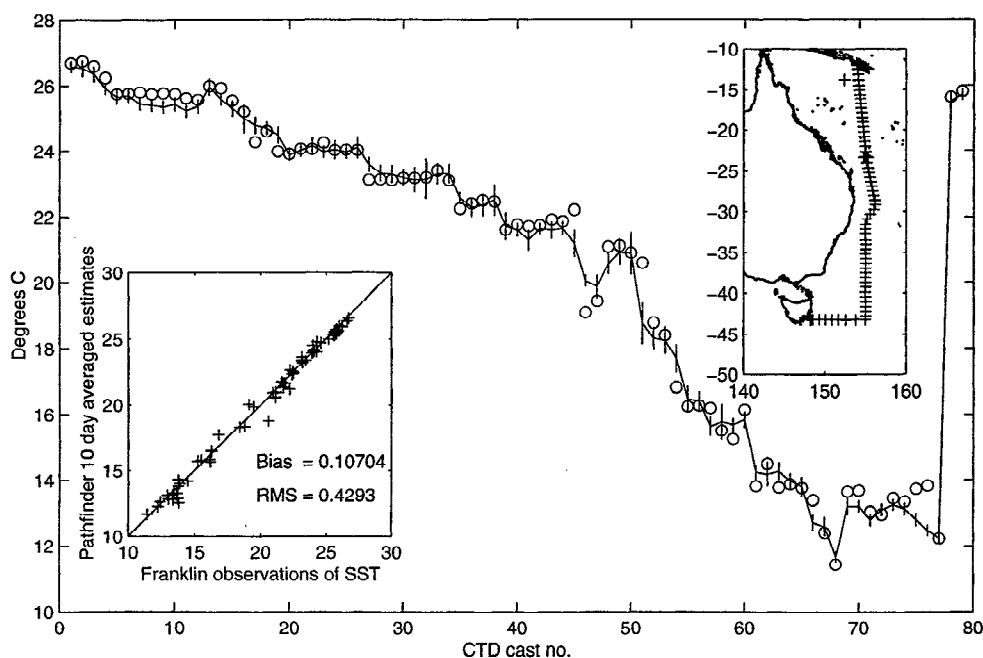

Figure 9. Ten-day Pathfinder SST analysis (solid line) with expected error bars compared to surface conductivity-temperature-depth (CTD) observations (circles), plotted by station number. Insets show scatter diagram of analysis estimates and CTD observations and R/V *Franklin* cruise 9306 CTD station locations.
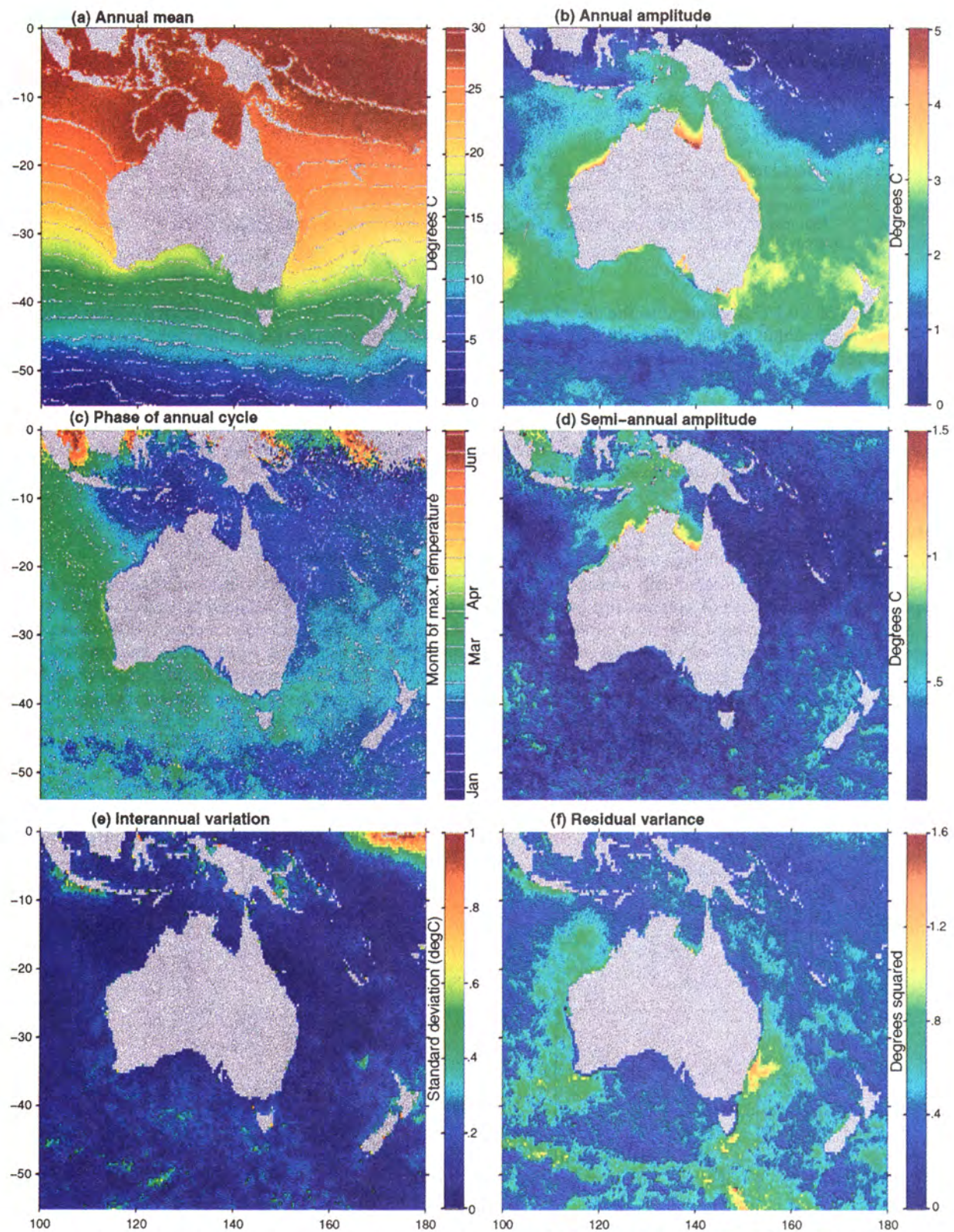
Plate 1. Background mean seasonal cycle and interannual variability fitted to the 1987–1994 Pathfinder SST data, in degrees Celsius. (a) Mean temperature. (b) Amplitude and (c) phase of the annual harmonic. (d) Amplitude of the semiannual harmonic. (e) Standard deviation of 365-day running mean filtered interannual variability. (f) Variance, in degrees Celsius squared, of the anomaly time series (i.e., difference between best SST and the fitted background field).
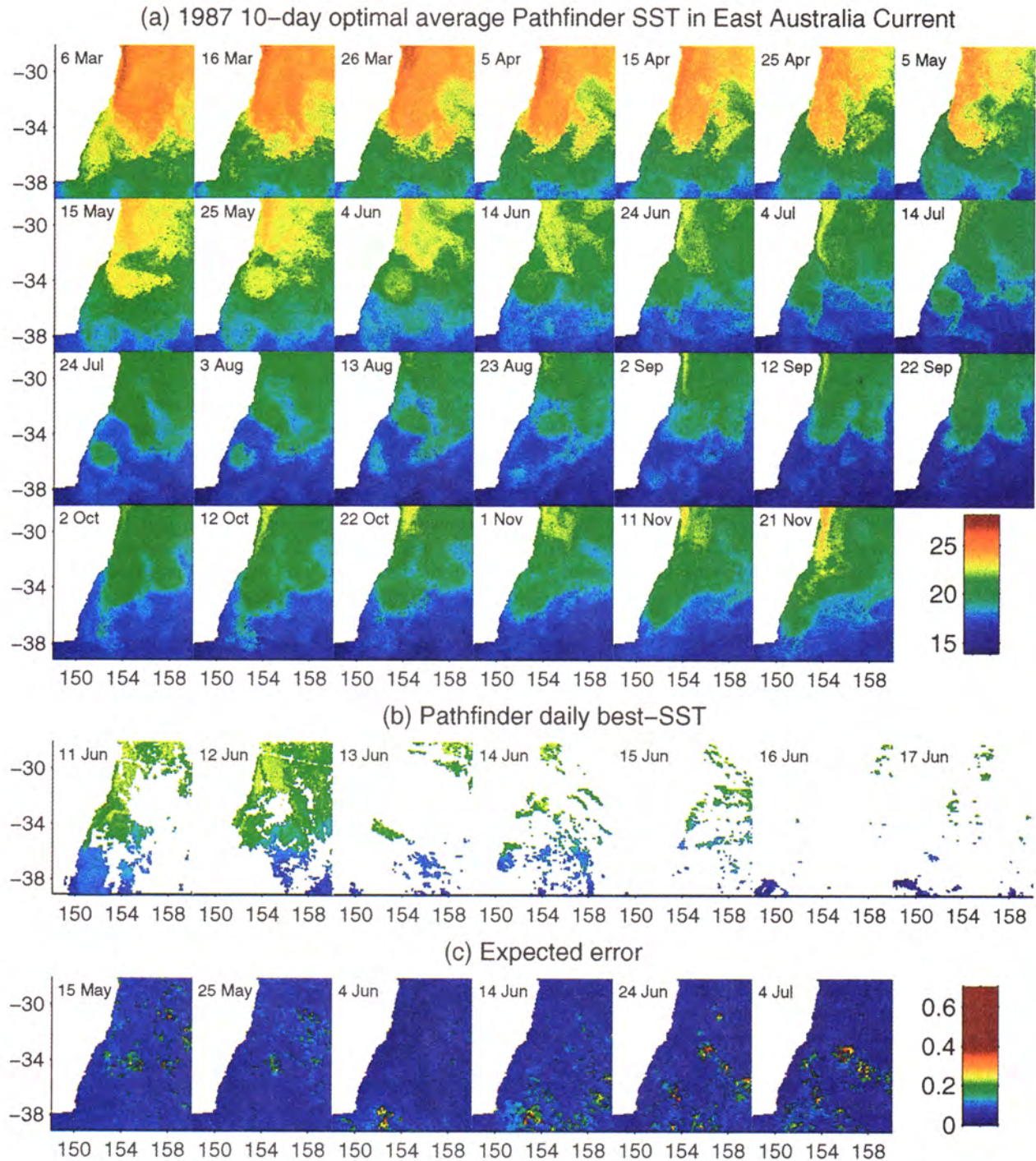
Plate 2. (a) Optimally averaged SST in degrees Celsius in the region of the East Australian Current separation during 1987. (b) The Pathfinder daily best SST data on 7 consecutive days spanning the June 14 estimate. Temperature scale for Plate 2b is the same as for Plate 2a. (c) Expected error for May 15 to July 4.
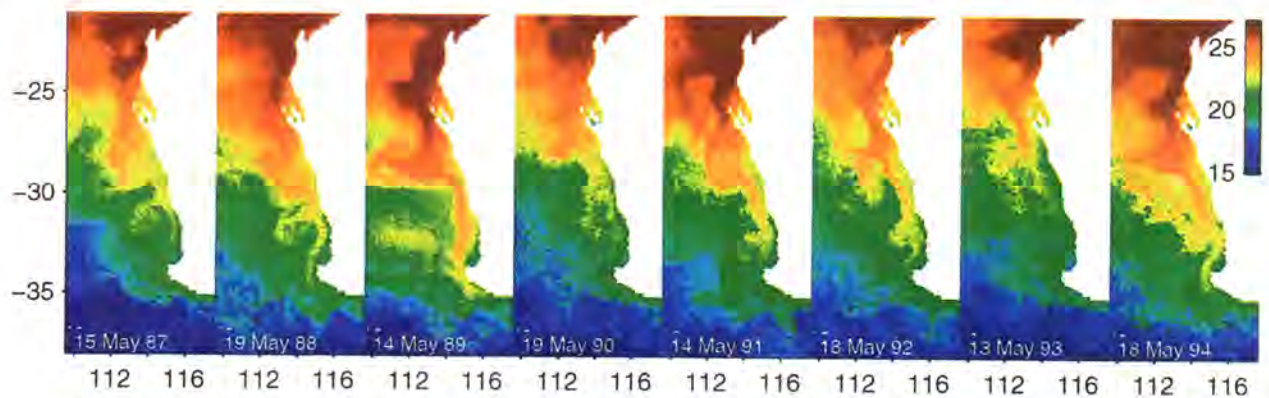
Plate 3. Optimally averaged SST in the Leeuwin Current region at the middle of May during each year 1987–1994. Temperature scale is in degrees Celsius.

wind mixing, but we have been unable to locate an open ocean SST time series that would allow us to verify this. However, we would not expect an effect appreciably different from that seen at 34°N in the Atlantic, where only some 20% of summer days show diurnal warming exceeding 0.5°C [*Stramma et al.*, 1986]. The strongest diurnal cycle observed in our region of interest is of the order of 3°C in the western equatorial Pacific [*Fairall et al.*, 1996] during cloud-free, low-wind conditions. At very low latitudes, then, it should be acknowledged that 10-day averages based on nighttime AVHRR data could be biased by the diurnal cycle. However, our comparison to TAO data (Figure 10) shows that at 10-day timescales there is no indication of a serious bias.

7. Ocean Circulation Features in the 10-Day Analyses

7.1. East Australian Current

Plate 2a shows SST at 10-day intervals in the region of the East Australian Current (EAC) separation during 1987. We present this sequence to show the types of mesoscale circulation events that the optimally averaged Pathfinder data resolve.

The start of the sequence shows the warmest waters separating from the coast at 32.5°S, as is frequently observed [*Godfrey et al.*, 1980], evidently encircling a high-geopotential feature. By April 15 a saddle forms in this ridge that pinches off completely by May 15 and rapidly evolves into a nearly circular warm-core eddy (May 25). Interaction with the shelf around June 24 may contribute to the appearance of streamers (filaments of warm water) emanating from the northwest and southeast perimeter of the eddy during July. Such streamers are associated with unstable breakup of anticyclonic eddies [*Griffiths and Pearce*, 1985b]. The eddy becomes distorted into an ellipse following further interaction with the shelf (August 13), and its SST signature eventually vanishes by September 12, a lifetime of over 3 months. After the first eddy separated, the warm water ridge was quickly reestablished (July 14), and a second eddy spawned on August 13. In contrast to the preceding event, this eddy coalesces with warm water from the north on September 22, while at the same time a third warm feature becomes distinct farther to the east, having evolved from a meander of the separated EAC. These two anticyclones drift slowly west and south and coalesce in early November, drawing warm water southward.

Eddy separation, coalescence, and dissipation events such as these are similar to those observed in other years with satellite imagery, satellite-tracked drifters, and shipboard observations [*Nilsson and Cresswell*, 1981; *Cresswell and Legeckis*, 1986]. With the Pathfinder data we have processed, it is possible to view this mesoscale variability continuously over a period of 8 years, without the confounding effect of clouds in the images. To illustrate the performance of the optimal averaging in spanning cloud gaps, Plate 2b shows the daily best SST for 7 consecutive days. On any given day the data gaps due to clouds are extensive, yet the optimal averaging procedure is able to extract from these data the signal of mesoscale circulation changes on timescales of 10 days.

Simple composite averaging of observations gives inferior results. *Chelton and Schlax* [1991] present a thorough comparison of the expected error of the two methods and for CZCS data show that mean expected ψ for optimal averages is typically half that of composite averages over the same interval. Figure 11 compares optimal and 30-day composite averaging for a time series at 162.4°E, 33.7°S in the EAC separation. A shorter composite averaging period is not practical because of the duration of data gaps. Little of the variability on 10-day timescales is resolved by the composite averages, and as a consequence, the evolution of mesoscale features in images corresponding to Plate 2a (not shown) is greatly obscured.

For completeness we show the expected error in the SST maps for May 15 through July 4, 1987, in Plate 2c. Errors of ±0.15°C are typical and seldom exceed ±0.4°C.

7.2. Leeuwin Current

The Leeuwin Current is fed predominantly by eastward flow of Indian Ocean subtropical waters. During early autumn the flow is augmented by warm waters from the northwest shelf that by May reach almost to Cape Leeuwin [*Smith et al.*, 1991]. Cyclonic and anticyclonic eddies spawned from large meanders in the current have been observed in local area coverage (LAC) AVHRR imagery [*Legeckis and Cresswell*, 1981; *Pearce and Phillips*, 1988] and were captured dramatically by drifter deployments in 1976 [*Cresswell*, 1977; *Cresswell and Golding*, 1980]. The optimally averaged SST during mid-May each year in 1987–1994 (Plate 3) shows that the pattern of meanders and eddies is similar from year to year. A meander showing some westward extension of warm northwest shelf waters is common at 25°S. Between 28° and 30°S a pronounced extrusion from the Leeuwin Current also evidently displaces waters westward
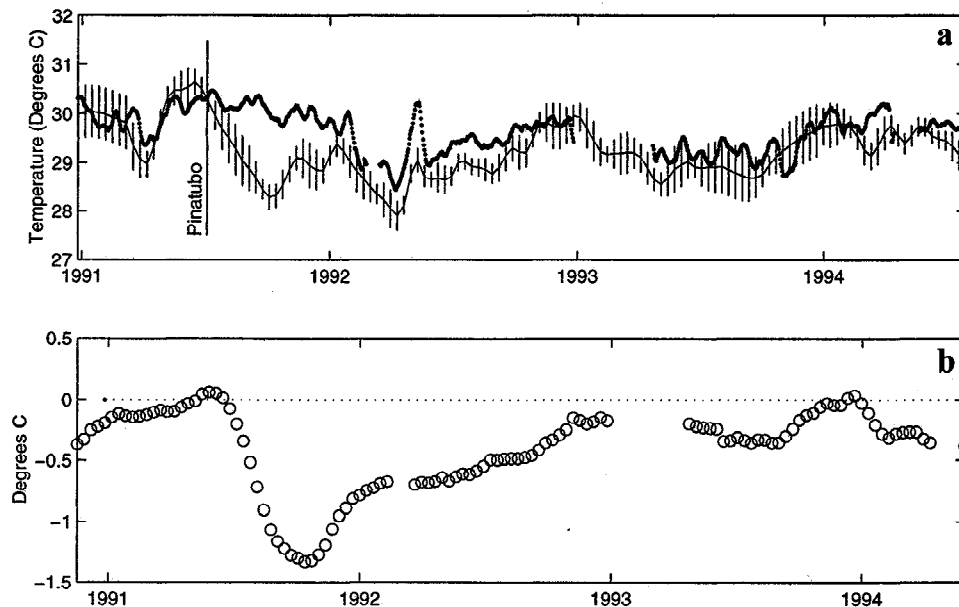
Figure 10. (a) Ten-day Pathfinder SST analysis (thin line) with expected error bars compared to 10-day low-pass time series from the Tropical Atmosphere-Ocean (TAO) mooring at 5°S, 165°E (thick line). (b) Difference of Pathfinder minus TAO.

each year. A feature of this nature, with strong eastward flow at its southern edge, carried drifters released offshore southeastward into the Leeuwin Current [*Cresswell and Golding*, 1980]. Near 33°S a warm anomaly, sometimes separated from the Leeuwin Current, occurs each year, though its latitude is more variable than the other features. Drifters have been trapped in this feature for 30–60 days, completing several circuits of the eddy before escaping [*Cresswell*, 1977].

When examined in detail, the scenes in Plate 3 commonly show cold cyclonic features of the order of 100-km diameter on the northern sides of the two southern warm meanders. The process of meander breaking through baroclinic instability leads to such cyclonic eddies being paired with separated warm anticyclones [*Griffiths and Pearce*, 1985a]. It has been speculated that variation in the strength, location, or timing of these mesoscale events may contribute to interannual variability in

the settlement of western rock lobster larvae in these waters [*Pearce and Phillips*, 1988].

8. Summary

In the Australian regional seas the cloud screening and quality control procedures applied by the Pathfinder analysis lead to gaps in the 9-km daily best SST data of median duration 3–5 days, with typically 60–80% of days having no SST value returned. Statistical interpolation by optimal averaging produces time series of best SST at the 9-km spatial resolution of the original data at an interval of 10 days, capturing considerable mesoscale SST variability in the result.

Deterministic cyclic and interannual variability in the data was estimated by fitting annual and semiannual harmonics and applying a 365-day running mean filter. These background
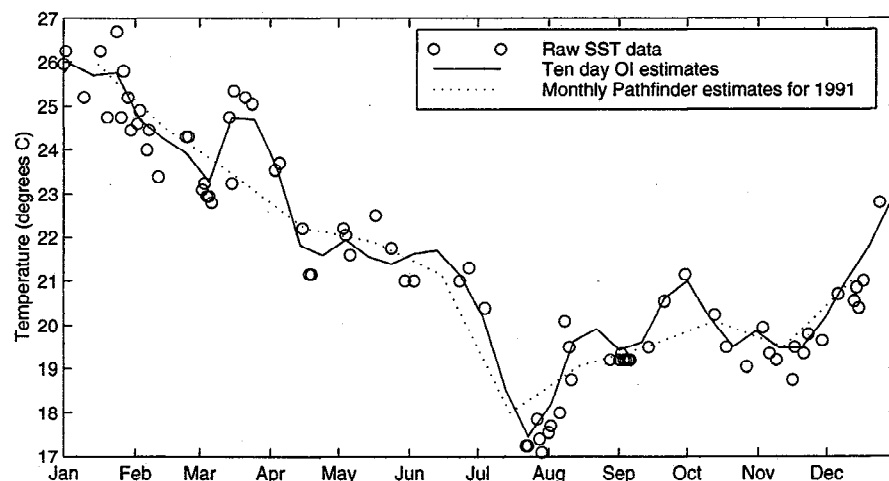
Figure 11. Ten-day optimal and 30-day composite average SST time series at 162.4°E, 33.7°S in the Tasman Sea.

time series at each point amount to an interannual and seasonal climatology for the data. Optimal averaging was applied in the time domain only to the anomaly between the data and the background time series. The background field shows considerable spatial structure near the 9-km resolution of the data that does not appear in other SST climatologies [Reynolds, 1988; Levitus and Boyer, 1994] that interpolate data horizontally as well as in time. Some short length scale features have distinct temporal signatures, such as interannual variability in the strength of Java coastal upwelling, local amplification of interannual SST variation at Wanganella Bank in the Tasman Sea, and the regular seasonal extension of the Leeuwin Current.

Once the background climatology is removed, a Markov function $(1 + \tau/a) \exp(-\tau/a)$ with timescale $a = 12$ days is a very good fit to the anomaly time series correlation function $\rho(\tau)$ everywhere in our region of interest. The noise variance was also stable geographically at $\sigma_e^2 = 0.15°C^2$, so that the noise to signal variance ratio λ could be computed from the data variance at each location using (8).

We have considered a region that extends from the tropics to high latitudes and includes boundary currents in two oceans. Our experience that $\rho(\tau)$ and σ_e^2 vary little over such a large domain suggests that our choices for these may well be used with SST data in other regions, with only a cursory check being required that they fit the anomaly time series. We emphasize, though, that the stability of ρ and σ_e^2 in our data are due in large part to the removal of the majority of the signal variance into the background field. Even the 365-day running mean filter plays a significant role here because without it, over 8 years of data, the anomaly correlation in some regions had a pronounced tail at very long lags; $\rho(100 \text{ days})$ would be of the order of 0.2 in the Great Australian Bight and northwest shelf. Removing interannual variability from the data to be optimally averaged alleviates the need to consider including this tail in the correlation function and also reduces the anomaly variance and therefore the expected error calculated from (7).

Selecting the averaging period $T = 10$ days was the least straightforward of our choices. Optimal interpolation is generally applied without averaging the correlation function, and we could have taken this approach. The averaging introduces a modest reduction in the expected error, with $\gamma = 0.95$ in (7) being typical, but the appeal of applying the averaging step is principally that for our applications we are interested in several-day timescales. If we had perfect uninterrupted daily SST data, we would still choose to filter this in time to make the data volume more manageable and to remove variability not relevant to the mesoscale processes in which we are primarily interested. We tried the shorter averaging period $T = 5$ days but succeeded only in smoothly interpolating the interval in the 10-day averaged time series. Estimates at the same time computed with $T = 5$ and $T = 10$ are barely distinguishable.

It might be expected that spanning temporal data gaps would be made easier by applying some horizontal interpolation, adding a spatial lag to ρ and including adjacent data points in the optimal average. This is not the case. The data gaps due to clouds are generally large contiguous areas (e.g., Plate 2b) so that relatively few of the points with no best SST are immediately adjacent to good data. Data at the edges of cloud regions may also contain a cold bias from undetected patchy cloud, and our experiments including spatial smoothing were unsuccessful.

Strictly speaking, our optimal averaging is suboptimal in the respect that we use a correlation function that is an approximation (though a very good one) to the true correlation, and we use an 80-day data window centered on the analysis time rather than all the data. By removing the majority of the long timescale variability to the background field, the weights α drop rapidly to zero with increasing lag. Limiting the data window, then, has negligible effect on the solution, yet the computation required in the repeated solution of (5) is dramatically reduced. To perform the optimal averaging of the 10^6 8-year time series in our region of interest took 3 days on a modern workstation.

The 10-day average estimates and error bars were validated by comparison with in situ data. In tropical TAO moorings an effect of the Mount Pinatubo eruption was apparent; however, the higher-latitude buoy and CTD data show no Mount Pinatubo biases and neither do comparisons with XBT data from volunteer observing vessels in the Tasman Sea (data not shown). The buoys show no systematic spatial or temporal trend in errors that might indicate gross errors in the SST algorithm. A chi-square goodness-of-fit test was applied to see whether the estimated error bars on the optimally averaged Pathfinder data were consistent with the probability distribution of the in situ data. The discrepancy between Pathfinder and in situ estimates was too large to be explained by the expected error bars for only one of the five time series long enough to perform the chi-square test. We therefore consider the estimated errors to be reasonable indicators of the accuracy of the 10-day average SST.

We have presented here results indicative of the features of Indo-Australian regional mesoscale circulation that the analysis captures. The EAC example shows that 10-day averages resolve the temporal evolution of mesoscale events, while the Leeuwin Current example indicates the value of the full 8-year data set in studying the interannual regularity of mesoscale variability. The results are well suited to applications, such as high-resolution ocean and atmosphere modeling, where the timescales and space scales of interest are of the order of 10 days and 9 km and for which the presence of gaps due to clouds is problematic.

References

Belkin, I. M., and A. L. Gordon, Southern Ocean fronts from the Greenwich meridian to Tasmania, *J. Geophys. Res.*, *101*, 3675–3696, 1996.

Bendat, J. S., and A. G. Piersol, *Measurement and Analysis of Random Data*, 146 pp., John Wiley, New York, 1966.

Bennett, A. F., The South Pacific including the East Australian Current, in *Eddies in Marine Science*, edited by A. Robinson, pp. 219–244, Springer-Verlag, New York, 1983.

Bretherton, F. P., R. E. Davis, and C. B. Fandry, A technique for objective analysis and design of oceanographic experiments applied to MODE-73, *Deep Sea Res., Oceanogr. Abstr.*, *23*, 559–582, 1976.

Chelton, D. B., and M. G. Schlax, Estimation of time averages from irregularly spaced observations: With application to coastal zone color scanner estimates of chlorophyll concentration, *J. Geophys. Res.*, *96*, 14,669–14,692, 1991.

Cresswell, G. R., The trapping of two drifting buoys by an ocean eddy, *Deep Sea Res.*, *24*, 1203–1209, 1977.

Cresswell, G. R., and T. J. Golding, Observations of a southflowing current in the southeastern Indian Ocean, *Deep Sea Res., Part A, 27,* 449–466, 1980.

Cresswell, G. R., and R. Legeckis, Eddies off southeastern Australia, *Deep Sea Res., Part A, 33,* 1527–1562, 1986.

Denman, K. L., and H. J. Freeland, Correlation scales, objective mapping and a statistical test of geostrophy over the continental shelf, *J. Mar. Res., 43,* 517–539, 1985.

Fairall, C. W., E. F. Bradley, J. S. Godfrey, G. A. Wick, J. B. Edson, and G. S. Young, Cool-skin and warm-layer effects on sea surface temperature, *J. Geophys. Res., 101,* 1295–1308, 1996.

Franke, R., Sources of error in objective analysis, *Mon. Weather Rev., 113,* 260–270, 1985.

Gandin, L. S., *Objective Analysis of Meteorological Fields* (in Russian), Gidrometeoizdat, St. Petersburg, Russia, 1963. (English translation, 242 pp., Isr. Program for Sci. Transl., Jerusalem, 1965.)

Gentilly, J. A., Thermal anomalies in the eastern Indian Ocean, *Nature Phys. Sci., 238,* 93–95, 1972.

Godfrey, J. S., The effect of the Indonesian throughflow on ocean circulation and heat exchange with the atmosphere: A review, *J. Geophys. Res., 101,* 12,217–12,237, 1996.

Godfrey, J. S., G. R. Cresswell, T. J. Golding, and A. F. Pearce, The separation of the East Australian Current, *J. Phys. Oceanogr., 10,* 430–440, 1980.

Griffiths, R. W., and A. F. Pearce, Instability and eddy pairs on the Leeuwin Current south of Australia, *Deep Sea Res., Part A, 32,* 1511–1534, 1985a.

Griffiths, R. W., and A. F. Pearce, Satellite images of an unstable warm eddy derived from the Leeuwin Current, *Deep Sea Res., Part A, 32,* 1371–1380, 1985b.

Legeckis, R., and G. R. Cresswell, Satellite observations of sea-surface temperature fronts off the coast of western and southern Australia, *Deep Sea Res., Part A, 28,* 297–306, 1981.

Levitus, S., and T. P. Boyer, *World Ocean Atlas 1994,* vol. 4, *Temperature, NOAA Atlas NESDIS 4,* 117 pp., Natl. Oceanogr. Data Cent., Silver Spring, Md., 1994.

McIntosh, P. C., Oceanographic data interpolation: Objective analysis and splines, *J. Geophys. Res., 95,* 13,529–13,541, 1990.

Nilsson, C. S., and G. R. Cresswell, The formation and evolution of East Australian Current warm-core edies, *Prog. Oceanogr., 9,* 133–183, 1981.

Pearce, A. F., and B. F. Phillips, ENSO events, the Leeuwin Current, and larval recruitment of the western rock lobster, *J. Cons. Cons. Int. Explor. Mer., 45,* 13–21, 1988.

Reynolds, R. W., A real-time global sea surface temperature analysis, *J. Clim., 1,* 75–86, 1988.

Reynolds, R. W., Impact of Mount Pinatubo aerosols on satellite-derived sea surface temperature, *J. Clim., 6,* 768–774, 1991.

Schahinger, R. B., Structure of coastal upwelling events observed off the south-east coast of south Australia during February 1983–April 1984, *Aust. J. Mar. Freshwater Res., 38,* 439–459, 1987.

Seaman, R. S., and M. F. Hutchinson, Comparative real data tests of some objective analysis methods by withholding observations, *Aust. Meteorol. Mag., 33,* 37–46, 1985.

Smith, E., J. Vazquez, A. Tran, and R. Sumagaysay, Satellite-derived sea surface temperature data available from the NOAA/NASA Pathfinder program, *Eos Trans. AGU Electron. Suppl.,* April 2, 1996. (Available as http://www.agu.org/eos_elec/95274e.html).

Smith, R. L., A. Huyer, J. S. Godfrey, and J. A. Church, The Leeuwin Current off western Australia, 1986–1987, *J. Phys. Oceanogr., 21,* 323–345, 1991.

Sprintall, J., D. Roemmich, B. Stanton, and R. Bailey, Regional climate variability and ocean heat transport in the southwest Pacific Ocean, *J. Geophys. Res., 100,* 15,865–15,871, 1995.

Stanton, B. R., An oceanic frontal jet near the Norfolk Ridge northwest of New Zealand, *Deep Sea Res., Oceanogr. Abstr., 23,* 821–829, 1976.

Stanton, B. R., The Tasman Front, *N.Z. J. Mar. Freshwater Res., 13,* 201–214, 1979.

Stramma, L., P. Cornillon, R. A. Weller, J. F. Price, and M. G. Briscoe, Large diurnal sea surface temperature variability: Satellite and in situ measurements, *J. Phys. Oceanogr., 16,* 827–837, 1986.

Tomczak, M., and J. S. Godfrey, *Regional Oceanography: An Introduction,* 422 pp., Elsevier, New York, 1994.

A. E. Walker, Woods Hole Oceanographic Institute, Woods Hole, MA 02543. (e-mail: awalker@whoi.edu)

J. L. Wilkin, School of Environmental and Marine Sciences, Tamaki Campus, University of Auckland, Private Bag 92019, Auckland, New Zealand. (e-mail: jl.wilkin@auckland.ac.nz)